Research

Authors for correspondence:
H. S. Fisher
e-mail: hsfisher@umd.edu
L. Giomi
e-mail: giomi@lorentz.leidenuniv.nl

Cellular geometry controls the efficiency of motile sperm aggregates

D. J. G. Pearce[1], L. A. Hoogerbrugge[1,2], K. A. Hook[3], H. S. Fisher[3] and L. Giomi[1]

[1]Instituut-Lorentz, Universiteit Leiden, PO Box 9506, 2300 RA Leiden, The Netherlands
[2]Kavli Institute of Nanoscience, Delft University of Technology, Delft, The Netherlands
[3]Department of Biology, University of Maryland College Park, MD 20742, USA

KAH, 0000-0001-5864-0316; HSF, 0000-0001-5622-4335; LG, 0000-0001-7740-5960

Sperm that swim collectively to the fertilization site have been observed across several vertebrate and invertebrate species, with groups ranging in size from sperm pairs to massive aggregates containing hundreds of cells. Although the molecular mechanisms that regulate sperm–sperm adhesion are still unclear, aggregation can enhance sperm motility and thus offer a fertilization advantage. Here, we report a thorough computational investigation on the role of cellular geometry in the performance of sperm aggregates. The sperm head is modelled as a persistent random walker characterized by a non-trivial three-dimensional shape and equipped with an adhesive region where cell–cell binding occurs. By considering both, a simple parametric head shape and a computer reconstruction of a real head shape based on morphometric data, we demonstrate that the geometry of the head and the structure of the adhesive region crucially affects both the stability and motility of the aggregates. Our analysis further suggests that the apical hook commonly found in the sperm of muroid rodents might serve to shield portions of the adhesive region and promote efficient alignment of the velocities of the interacting cells.

1. Introduction

In most species, the number of sperm available for fertilization far outnumber ova, which gives rise to fierce competition at the cellular scale [1]. The highly efficient and streamlined shape of most sperm cells is the product of intense selective pressure to improve swimming performance. In a rare number of systems, sperm form cooperative groups, or aggregates [2–6]; this fascinating behaviour is believed to improve the swimming performance of the cells involved, compared to individual cells, and therefore the chances of successful fertilization [6]. Yet, *in vitro* studies have shown inconsistent results [3] and the underlying physics of the associations remains elusive [7–9].

Among mammals, the natural variation observed within muroid rodents [10] offers important insight into how cell shape and orientation can mediate collective motion of sperm. For example, the sperm of house mice (*Mus musculus*) form groups in which the head of a sperm is bound to either the head or the tail of another cell, whereas in the Norway rat (*Rattus norvegicus*), sperm form comet-like aggregates in which all the cells are bound at the head and preserve the head-tail directionality of a single cell [11]. These morphological variations result in a substantial difference in the aggregate swimming performance: while in the Norway rat, sperm groups swim faster than single cells, no speed advantage is found in the house mouse. Train-like aggregates are also found in the wood mouse (*Apodemus sylvaticus*), where aggregation is known to improve swimming performance [2]. In most muroid rodents, sperm have a falciform head with an apical hook that is thought to facilitate the formation [2] and/ or stabilization [11] of aggregates, although other scenarios have also been suggested [12]. Although the molecular mechanisms that regulate sperm–sperm adhesion in these systems are not well understood, in house mice,

transmembrane glycoproteins more typically associated with sperm-egg binding are probably involved [13].

In previous work, we studied sperm from *Peromyscus* rodents and analysed how the swimming velocity of the aggregates is modulated by group size [14]. By combining fine-scale imaging of living cells and a simple two-dimensional mechanical model of sperm aggregates (inspired by the Vicsek model [15] and the statistical mechanics approach to collective behaviour [16–24]), we demonstrated that the average velocity of an aggregate does indeed increase with its size as the group moves more persistently. This benefit, however, is offset in larger aggregates as the geometry of the group forces sperm to swim against one another. This result is a non-monotonic relationship between aggregate size and average velocity with an optimum that is predominantly determined by the geometry of the sperm head [14]. The underlying mechanism leading to this optimality is straightforward: by forming tightly packed head-to-head aggregates, sperm are able to ease each other's directional fluctuations by sterically restraining one another. This results in a straighter trajectory, thus a greater average velocity. Large aggregates, however, tend to be isotropic and this forces the sperm to swim against one another, thus reducing the aggregate speed.

In this work, we report a thorough computational investigation on the role of cellular geometry in the performance of sperm aggregates, as well as on the structure of the adhesive region of the cell head. For this purpose, the sperm head is modelled as an ellipsoid of revolution. Although considerably less structured than the actual head shape found in most muroid rodents, this is a simple parametric shape with enough morphological features (e.g. slenderness, oblateness, etc.) and provides insight into the effect of the head shape on the spatial organization and the motility of the aggregates. Furthermore, with the help of a data-based computer reconstruction of a *Peromyscus maniculatus* sperm head, we explore the interplay between the geometry of the apical hook and the structure of the adhesive region, and identify a number of highly efficient configurations that could provide a basis for future experimental studies.

2. The model

Our computational model aims to reproduce the physical interactions between sperm cells arising from steric repulsion and linkage through adhesive molecules. Each cell is modelled as a persistent random walker in three dimensions (e.g. [25]), subject to a constant propulsive force and a random torque, and whose dynamics is governed by the overdamped Newton equations. When two sperm cells come into contact they experience a repulsive force, sufficient to prevent them from overlapping, as well as an attractive force reproducing the effect of adhesive molecules. The sperm head is modelled as a three-dimensional simplex: a set of triangles connected along the edges in such a way to form a closed polyhedron. This allows us to reproduce any desired morphological features including the apical hook found in the sperm cells of most muroid rodents [10]. The simplest non-trivial three-dimensional shape suitable for a geometrical model of the sperm head is the ellipsoid of revolution (figure 1a). Although less complex than the typical
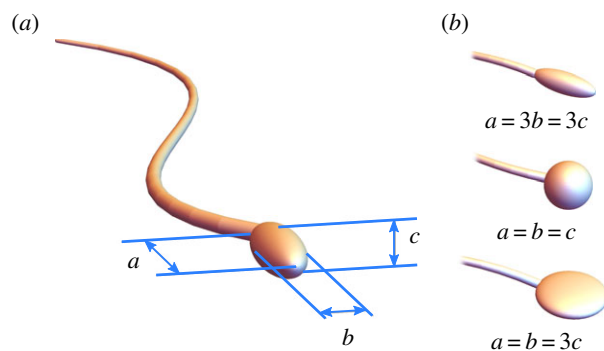
Figure 1. (a) Schematic of the geometrical model used in the simulations. The cell's head is represented as an ellipsoid whose axes are *a*, *b* and *c*. (b) Upon adjusting the ratios *b/a* and *c/a*, one can reproduce various head morphologies. The tail serves to mark the highlight the orientation of the head with respect to the direction of motion of the cell, but it is not included in the geometrical model. (Online version in colour.)

head shape found in rodents, this is a simple and yet sufficiently rich parametric shape, whose morphological feature can be entirely described in terms of the three parameters *a*, *b* and *c* (figure 1a). Adjusting the ratio between these lengths permits us to reproduce various kinds of shapes (figure 1b).

At each time-step *t*, the location and orientation of the head of the generic *i*th sperm cell are described by the position $r_i(t)$ of the head centre of mass and the direction $p_i(t) = \hat{R}_i(t) \cdot p_i(0)$ of the head major axes, with $\hat{R}(t)$ a 3×3 rotation matrix and $p(0)$ the direction at $t = 0$. These quantities are then iteratively updated by means of the following recursive equations:

$$r_i(t + \Delta t) = r_i(t) + \Delta t[v_0 p_i(t) + \mu_t F_i(t)] \quad (2.1a)$$

and

$$\hat{R}_i(t + \Delta t) = \hat{R}_i(t) \cdot \hat{T}_i(t). \quad (2.1b)$$

The term $v_0 p_i$ in equation (2.1a) represents the self-propulsion provided by the beating of the tail, μ_t is a mobility constant and F_i expresses the total force experienced by the *i*th head. In turn, this can be decomposed as:

$$F_i = \sum_{j=1}^{N_c} F_{ij}^c + \sum_{j=1}^{N_a} F_{ij}^a, \quad (2.2)$$

where F_i^c and F_i^a are, respectively, the forces resulting from the steric and adhesive interactions between the *i*th sperm head and other heads, we have dropped time-dependence for sake of conciseness. N_c is the number of cells in contact with the *i*th, while N_a is the number of cells connected to the *i*th by an adhesion molecule. Finally, $\hat{T}_i$ is a 3×3 matrix, that embodies the rotation caused by torque experienced by the *i*th sperm head.

Steric interactions are resolved by locating the intersections between the triangles comprising the three-dimensional model of the head. This task is performed using the C^{++} library RAPID [26]. Once a collision is detected, we reconstruct the volume defined by the intersection between the overlapping heads. The position r_{ij}^c of the centre of mass of such a volume is identified as the location of the collision between the *i*th and *j*th cell (figure 2a). The associated steric force F_{ij}^c is parallel to the spatially averaged surface normal, N_{ij}, of the intersecting regions, while its magnitude is set to be
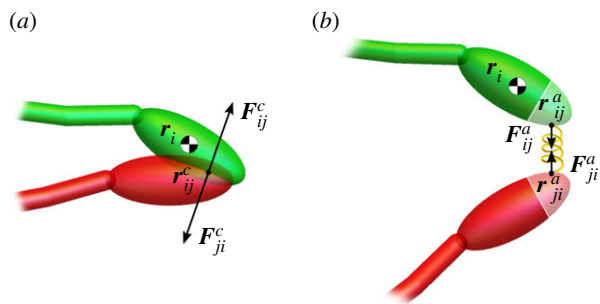
Figure 2. Schematic of the head–head interaction used in the numerical model. Each cell head is subject to a steric force (a), resulting from the collision with other heads, and an attractive force (b), owing to cell–cell adhesion. The latter is modelled as a linear spring force and is switched on once the heads adhesive regions (highlighted) are closer than a given threshold. (Online version in colour.)

proportional to $v_0 \Delta t$. The force and torque on the ith cell resulting from the steric interaction with the jth cell are therefore given by the expressions:

$$\boldsymbol{F}_{ij}^c = \kappa_c v_0 \Delta t \boldsymbol{N}_{ij} \qquad (2.3a)$$

and

$$\boldsymbol{\tau}_{ij}^c = (\boldsymbol{r}_{ij}^c - \boldsymbol{r}_i) \times \boldsymbol{F}_{ij}^c, \qquad (2.3b)$$

where κ_c is the elastic constant.

Cell–cell adhesion is modelled by a spring-like adhesion molecule. These adhesion molecules are localized to specific regions on the surface of the sperm head, and, if the regions come within an interaction distance l_a, a tether is formed between the heads (figure 2b). This is achieved by finding the closest pair of vertices within the adhesive region of the ith and jth cell, whose positions are $\boldsymbol{r}_{ij}^a$ and $\boldsymbol{r}_{ji}^a$, respectively, and connecting them with a Hookean spring. The spring has finite strength and will break if $|\boldsymbol{r}_{ij}^a - \boldsymbol{r}_{ji}^a| > l_a$. The force and torque on the ith cell resulting from the adhesive interaction with the jth cell are then:

$$\boldsymbol{F}_{ij}^a = \kappa_a(\boldsymbol{r}_{ij}^a - \boldsymbol{r}_{ji}^a) \qquad (2.4a)$$

and

$$\boldsymbol{\tau}_{ij}^a = (\boldsymbol{r}_{ij}^a - \boldsymbol{r}_i) \times \boldsymbol{F}_{ij}^a, \qquad (2.4b)$$

where κ_a is a second elastic constant.

The angular velocity of the ith sperm head is determined, under the assumption of overdamped rotational dynamics, by the combination of $\boldsymbol{\tau}_{ij}^c$ and $\boldsymbol{\tau}_{ij}^a$, as well as by a stochastic contribution reproducing the effect of the noisy flagellar motion, namely:

$$\boldsymbol{\omega}_i = \mu_r \left(\sum_{j=1}^{N_c} \boldsymbol{\tau}_{ij}^c + \sum_{j=1}^{N_a} \boldsymbol{\tau}_{ij}^a \right) + \eta \boldsymbol{\xi}_i, \qquad (2.5)$$

where μ_r a rotational mobility coefficient, $\boldsymbol{\xi}_i$ is a randomly oriented vector uniformly sampled from the unit sphere and η is a constant, controlling the magnitude of the rotational noise. The choice of white noise here is motivated by the fact that, in most aggregating sperm (with some relevant exceptions, such as in the case of the opossum [27,28] or the fishfly *Parachauliodes japonicus* [29]) the beating of the tails occurs asynchronously (see also [30] for a deterministic model of torque induced by the tail oscillations). Finally, taking $\boldsymbol{\omega} = (\Delta\theta/\Delta t)\boldsymbol{k}$, with $\boldsymbol{k}$ a unit

vector, and using Rodrigues' rotation formula, we obtain the rotation matrix

$$\hat{\boldsymbol{T}} = \hat{\boldsymbol{I}} + \sin\Delta\theta \hat{\boldsymbol{K}} + (1 - \cos\Delta\theta)\hat{\boldsymbol{K}}^2, \qquad (2.6)$$

where $\hat{\boldsymbol{I}}$ is the identity matrix and $\hat{\boldsymbol{K}}$ is the matrix of column vectors resulting from the cross product between the Cartesian basis vectors and unit vector $\boldsymbol{k}$, namely:

$$\hat{\boldsymbol{K}} = \begin{pmatrix} 0 & -k_z & k_y \\ k_z & 0 & -k_x \\ -k_y & k_x & 0 \end{pmatrix}. \qquad (2.7)$$

Consistent with the experimental evidence about the role of hydrodynamics in sperm aggregation, we choose to ignore hydrodynamic interactions. As it was demonstrated by Fisher and Hoekstra with *Peromyscus*, aggregation occurs predominantly between sperm of the same male, even when tested with sperm from a full-sibling litter-mate [5]. This behaviour supports the assumption that hydrodynamic interactions must have a secondary role, if any, compared to biochemical ones. Furthermore, in [7], it was shown using a two-dimensional model, that aggregates held together by hydrodynamic interactions swim more slowly than individual sperm. Thus the opposite of what is observed in *Peromyscus*.

In all simulations presented here, we set the time and length units by choosing $\Delta t = 1$ and $a = 1$. The remaining free parameters are then set as follows: speed of the particle $v_0 = 0.01$, rotational noise amplitude $\eta = 0.05$, rotational mobility coefficient $\mu_r = 0.1$, translational mobility coefficient $\mu_t = 1$, steric spring constant $\kappa_c = 0.1$, adhesion spring constant $\kappa_a = 0.1$ and maximum length of the tether $l_a = 0.1$. For parameterized cell shapes, we use a triangulation consisting of 100 vertices forming 196 triangles. For the more accurate cell models, we use 201 vertices resulting in a mesh of 400 triangles. The adhesion points are defined on the same mesh, with triangles being designated either adhesive or not. The simulations are initialized by placing the cells at random positions with random orientations within a small region. Overlaps between the cells are removed and the density is increased to form an aggregate. The simulations then undergo 10^5 equilibration steps to obtain a stable configuration before starting the measurements. We assume ergodic behaviour in our simulations and unless stated otherwise, results presented are based on a single simulation of at least $t = 10^7$ time steps.

3. Results

3.1. Aggregates travel faster than individual cells

Each individual *in silico* sperm swims forward while undergoing rotational diffusion, mimicking the erratic swimming behaviour of real sperm. There is no preferred direction or target in the simulation, therefore sperm cells perform a persistent random walk (figure 3a). This motion is characterized by a short-time ballistic regime, in which the mean square displacement of the centre of mass of the aggregate scales quadratically with time (i.e. $\langle R^2(t)\rangle \sim t^2$, where the angular brackets indicate a statistical average), and a diffusive regime, in which $\langle R^2(t)\rangle \sim t$. The ballistic motion occurs over a time interval that is shorter than or comparable to the reorientation time of the sperm. The diffusive regime, on the other hand, is found when the time interval is greater than the reorientation time of the sperm (figure 3b).
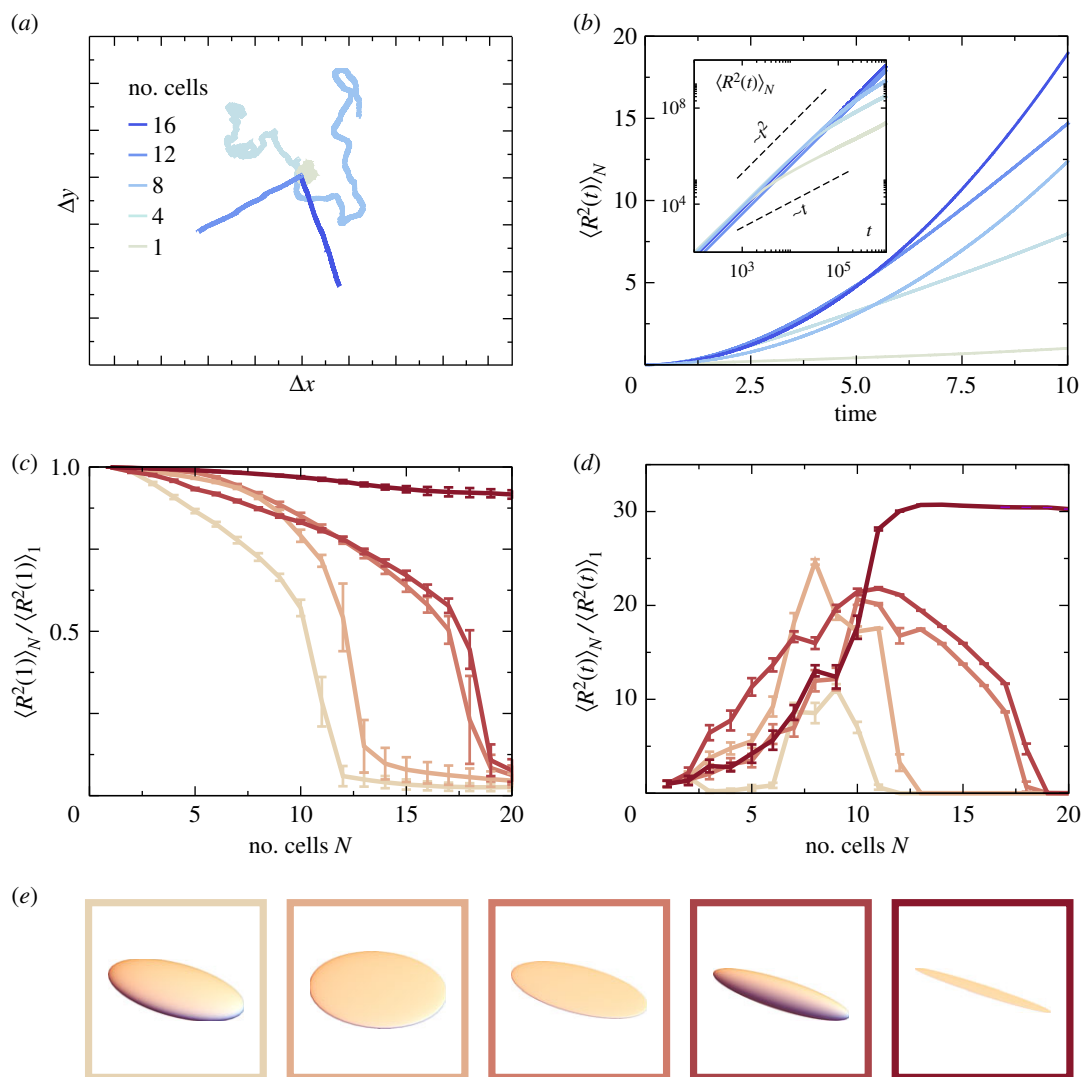
Figure 3. (a) Trajectories of five different aggregates with $N = 1, 4, 8, 12$ and 16. Upon increasing in size, the aggregates become progressively more persistent, because of the reduced fluctuations in the aggregates average direction ($b/a = 0.2$, $c/b = 1$). (b) Mean square displacement $\langle R^2(t)\rangle_N$ versus time for the same five aggregates of size N. (Inset) same data on logarithmic scale. As characteristic of persistent random walkers, the aggregate crossover from a ballistic regime, where $\langle R^2(t)\rangle_N \sim t^2$, to a diffusive one, where $\langle R^2(t)\rangle_N \sim t$. (c) Instantaneous speed of an aggregate relative to a single cell versus the number of cells in the group for various aspect ratios b/a and c/a. This is calculated as the mean square displacement after one time step normalized by the same value for a single cell: i.e. $\langle R^2(1)\rangle_N/\langle R^2(1)\rangle_1$. Regardless of the aspect ratio, the instantaneous speed of an aggregate decreases monotonically as this becomes more isotropic, hence cells swim against each other. This effect is more pronounced for isotropic head shapes, whereas is barely visible for highly anisotropic cells. (d) Relative mobility increase for an aggregate versus the number of cells in an aggregate, for the same aspect ratio values. This is calculated as the long-time mean square displacement ($t = 10^5$) normalized by the same value for a single cell. The increased persistence owing to aggregation results in a higher mobility of the aggregates. This benefit is offset in larger aggregates as the geometry of the group forces sperm to swim against one another. For these simulations, the adhesive region of the sperm cells is at the tip of the head. (e) Illustration of the head shapes used for (c,d). The parameter values used in the simulations are outlined in §2.

When many cells crowd together, the available space for each sperm head is restricted, leading to a reduction in the amount of rotational motion each sperm head experiences while swimming (figure 3a). This results in a longer reorientation time for a sperm aggregate, thus a larger persistence (figure 3b). As a consequence, the distance covered by a sperm aggregate within a given time interval is larger than in the case of individual cells, effectively making aggregates faster. Such a benefit, however, also depends on the travelling time. For instance, as shown in figure 3b, groups of $N = 4$ sperm cells are faster than groups of $N = 16$ only in short time periods, whereas this pattern reverses at longer durations.

Whereas the average velocity (i.e. $V(t) = \sqrt{\langle R^2(t)\rangle}/t$ for finite t) increases with the size N of the aggregates, their speed (i.e. limit of $V(t)$ for $t \to 0$) is a monotonically decreasing function of N. This originates from the fact that, owing to

their ellipsoidal shape, cells are always partially splayed towards the mean direction of motion of the aggregate. As a consequence, part of the propulsion provided by the swimming cells is lost, leading to a reduction in the instantaneous speed of the aggregate (figures 3c and 4). The instantaneous speed of all aggregates monotonically decreases with additional sperm cells, eventually reaching zero when groups have no net polarization and cannot move. This effect is far more pronounced in sperm with wider heads, because slender cells are able to pack more efficiently with nearly parallel orientations in far larger numbers.

To quantify the relative velocity increase caused by aggregation, we have compared the mean squared displacement of aggregates of different size at a fixed time $t = 10^5$ (figure 3d). Although limited to a specific time, this measure has the benefit of capturing both the advantages of the rotational
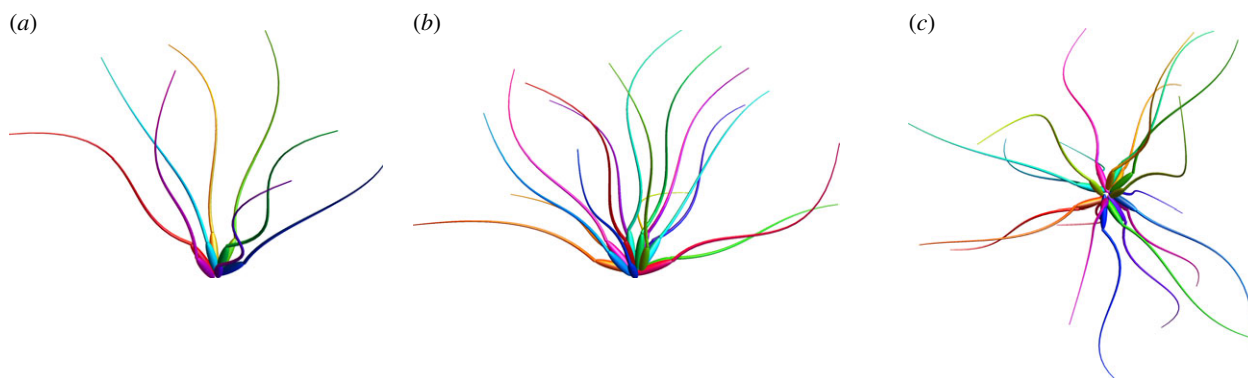
Figure 4. Images showing how the typical configurations of sperm aggregates change with number of cells obtained from a numerical solution of equations (2.1). (*a*) Here, $N = 8$ cells retain a high degree of polarization and the packing reduces rotational diffusion. (*b*) For $N = 16$ cells the total polarization is reduced, many cells on the periphery of the aggregate are pushing inwards rather than forwards. In this configuration, the rotational diffusion is very low but the speed is significantly reduced. (*c*) $N = 20$ cells arrange with no net polarization. The speed of the aggregate is now close to zero with no persistent direction. (Online version in colour.)
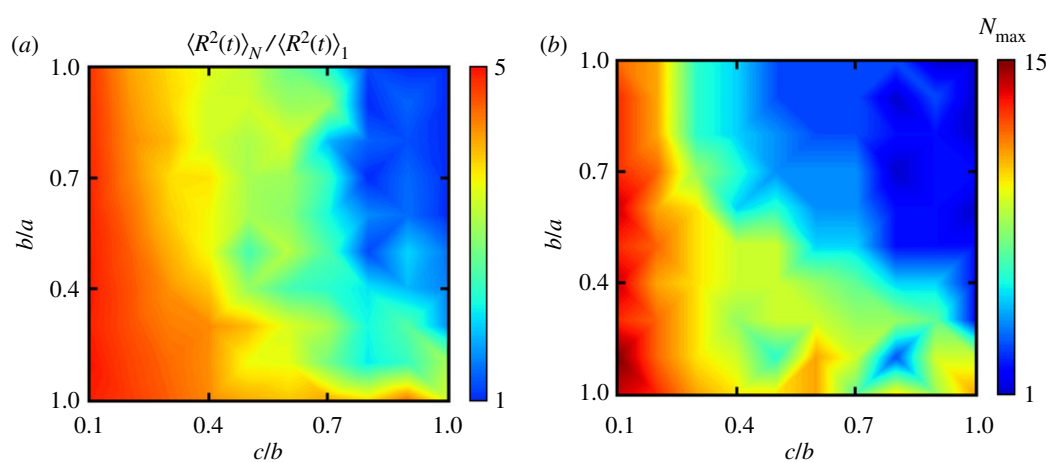
Figure 5. (*a*) Maximum speed increase of an aggregate of up to 20 sperm cells with different shaped heads. The speed increase is calculated as the mean squared displacement at $t = 10^5$ normalized by the same quantity for a single cell. (*b*) Optimum aggregate size (up to 20 cells) for sperm cells with different head shapes. For these simulations, the adhesive region of the sperm cells is at the tip of the head.

damping and the disadvantage of loss of instantaneous speed. This can then be combined with our direct measurements of the instantaneous speed to give a more complete picture of the behaviour of the aggregate.

We normalize mean squared displacement of the aggregates by that of an individual cell to obtain a relative velocity increase. With this choice of t, the optimal number of cells ranges between 7 and 10, with a maximum velocity increase of nearly thirty times. This behaviour exhibits strong dependence on the geometry of the sperm cell head, with slender cells generally exhibiting a far greater increase in distance travelled, which is true even for very large aggregates. The origin of this property is twofold: on the one hand, the instantaneous speed of the aggregate is higher for slender cells, as mentioned earlier. On the other hand, very prolate ellipsoids pack more efficiently than other shapes. This hinders the reorientation of the cells inside an aggregate, thus enhancing the rotational damping described earlier.

3.2. Head geometry strongly affects the performance of the aggregate

In order to shed light on the effect of sperm head geometry on the performance of motile aggregates, we performed simulations for a wide range of head aspect ratios (b/a and c/a) and aggregate size (N). Figure 5a shows the maximum relative velocity of an aggregate for different aspect ratios. It is immediately clear that the fastest aggregates contain cells with a smaller aspect ratio, owing to the fact that slender cells can form tightly packed aggregates where the velocities of the individual cells are roughly parallel. Interestingly, the strongest dependence observed here is on the second aspect ratio c/b, which implies that prolate (i.e. rod-like) and oblate (i.e. plate-like) heads have comparable efficiency upon aggregation. Intuitively, this originates from the fact that plate-like sperm heads are able to stack, thus increasing the alignment of the velocities of individual cells. Furthermore, for a given volume, plate-like heads have a significantly larger area than both spherical and rod-like heads, hence more space for membrane-bound adhesion molecules [10].

Figure 5b shows the optimal size of sperm aggregate for different shaped sperm cells. Consistent with the previous considerations, flatter sperm heads obtain the greatest advantage when they form larger aggregates, this again is owing to their ability to pack many cells effectively with highly aligned velocities. For very spherical sperm heads, there is no advantage to forming an aggregate, and we see that the optimal group size consists of a single cell (blue region in figure 5b).
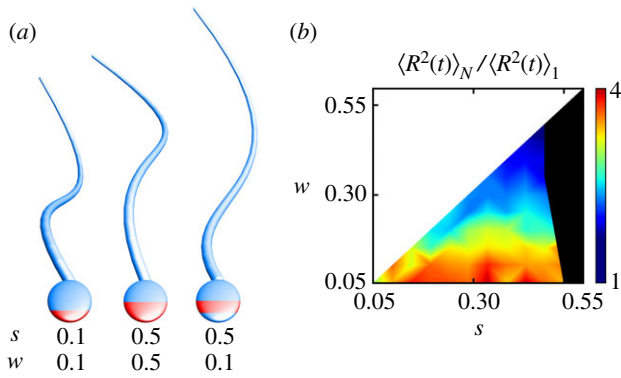
Figure 6. (*a*) The adhesive region of the sperm head (in red) can be parameterized by two lengths corresponding to the starting position *s* and the width *w*. (*b*) Velocity increase obtained from the simulations of five different variants associated with different values of *s* and *w*, calculated as the mean squared displacement at $t = 10^5$ normalized by the same quantity for a single cell. The best performance is obtained when the adhesive strip occupies a small portion of the sperm head. Conversely, an excessively large adhesive region can compromise the flexibility of the aggregates, resulting in a breakup of the aggregates. The aggregates in these simulations consist of $N = 5$ cells which each have the aspect ratios $b/a = 0.5$ and $c/b = 0.4$ to approximate the shape of *Peromyscus* sperm cells.

3.3. The structure of the adhesive region strongly affects the performance of the aggregate

The results reported in the previous two sections rely on the assumption that the adhesive portion of the sperm head is localized at the forward tip. In order to study how the structure of the adhesive region affects the performance of the aggregate we have simulated five variants with aspect ratio $b/a = 0.5$ and $c/b = 0.4$, which is close to features observed in *P. maniculatus* and *Peromyscus polionotus* [14]. We define the adhesive region as a strip that starts from a position *s* from the tip of the sperm head and extends towards the tip over a width *w*, i.e. when $s = w$ then the front of the sperm cell is covered in an adhesive cap that extends down to the tip, whereas if $s > w$ the adhesive region is limited to a band (figure 6*a*).

Figure 6*b* shows the typical velocity increase obtained from the simulations of the different variants. The best performance is obtained when the adhesive strip occupies a small portion of the sperm head. On the other hand, when the adhesive strip extends towards the tip, i.e. $s \sim w$, the advantage is somewhat lost. If the adhesive strip extends past the mid-region of the cell towards the tail, we see that the aggregates become unstable and break up over time, denoted by the black region on the right side of figure 6*b*.

This behaviour can be understood by considering the torque exerted on the sperm cells by the adhesion molecules. The adhesion molecules pull the adhesive region of neighbouring cells together. Since the cells cannot overlap, the point of contact between the cells acts like a fulcrum applying a torque to the sperm cell. When the adhesion molecule is towards the front of the sperm head, it will generally cause the orientations of the two cells to converge. As explained earlier, this can cause a slowdown of the group, but ultimately promotes adhesion as the resulting configuration has the particles swimming towards each other. If the adhesive region is towards the tail of the cell, the effect of the torque is for the velocities to diverge, resulting in a configuration in which the cells are swimming away from each

other and the aggregate eventually breaks up. This leads to the unstable region shaded black on figure 6*d*. Such an effect is amplified in wider cells as the point of contact is generally further from the centre line of the cell. The cells are generally fastest when the adhesion region is limited to a thin band round the cell. This is the configuration which generally minimizes the torque on the velocity of the cell, when the cells are parallel, leading to the fastest aggregates.

Although the breakup of the aggregate owing to the torque build-up is probably a property of the ellipsoidal head shape considered here, our results suggest that an efficient aggregation might require the cells to maintain some freedom to rotate in order to guarantee some degree of flexibility of the whole aggregate.

3.4. Aggregation performance of *Peromyscus maniculatus* from morphometric data

In this section, we extend our approach to account for more realistic head geometries. In particular, we consider the sperm cell of *P. maniculatus*. The purpose of this analysis is twofold. First, using realistic head geometries allows us to test the validity of the results presented in the previous sections and to demonstrate that many of the properties illustrated with the elliptical model are robust and carry over to realistic head geometries. Second, we explore the interplay between the geometry of the apical hook and the structure of the adhesive region and identify a number of highly efficient configurations that could provide a basis for future experimental studies.

Sperm samples were dissected from the epididymes of sexually mature males, fixed in 2.5% glutaraldehyde, dehydrated first in a graded ethanol series, then in hexamethyldisilazane, and sputter coated in gold/palladium. Samples were imaged on a Hitachi SU-3500 scanning electron microscope at the Laboratory for Biological Ultrastructure, University of Maryland (figure 7*a,c*). The two planar electron micrographs shown in figure 7*a,c* were first traced to create a general outline and identify the centre-line of the hook. This was then extruded to a three-dimensional model consisting of 400 triangles (figure 7*b*).

Sperm aggregates were simulated in small groups such as that imaged in figure 7*d*. To shed light on the interplay between the hook geometry and the structure of the adhesive region, we considered six different variants as shown in figure 8*a*. The instantaneous speed of the aggregates (figure 8*b*) is particularly sensitive to the structure of the adhesive region in the presence of the hook. Aggregates with the adhesive region covering only the mid-section or hook are able to maintain consistently high instantaneous speeds, whereas sperm cells where the adhesive region extends beyond the midpoint of the head are significantly slower (figure 8*b*). At longer time scales the difference between the aggregates is even more pronounced, with sperm cells having an adhesive cap on the forward section of the head being the fastest and sperm cells with the whole body adhesive being the slowest (figure 8*c*). These behaviours are rooted in the physical mechanism outlined in §3.3. The torques applied by the adhesion molecules are not necessarily promoting alignment unless limited to the upper half of the sperm head. The *P. maniculatus* sperm head is substantially flat, with two large roughly parallel sides which reduce the torque exerted by adjacent sperm, allowing for very efficient stacking. This cell shape reduces the crowding
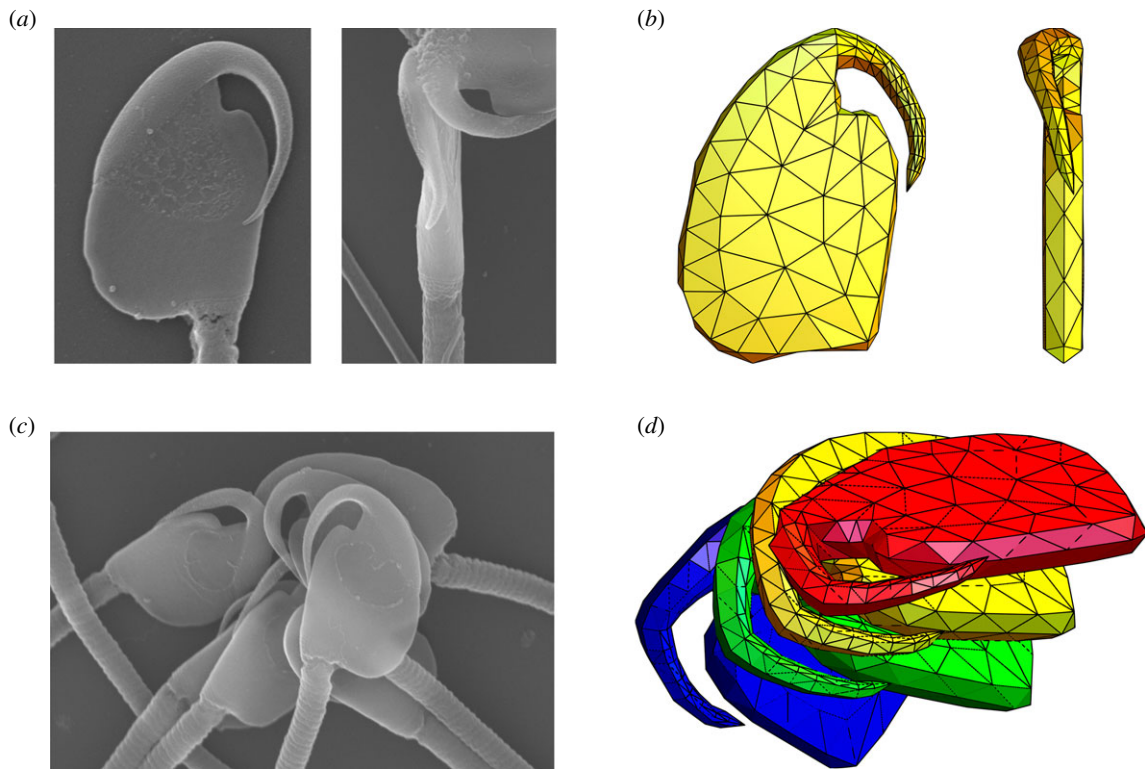
Figure 7. (a) Electron micrographs of sperm from *P. maniculatus*, a species in which sperm aggregate [14]. (b) Planar views of the sperm head model constructed from the morphometric data. (c) Electron micrograph of an aggregate of *P. maniculatus* sperm cells. (d) A snapshot from a simulation of a group of four sperm heads using a more realistic model head shape. (Online version in colour.)
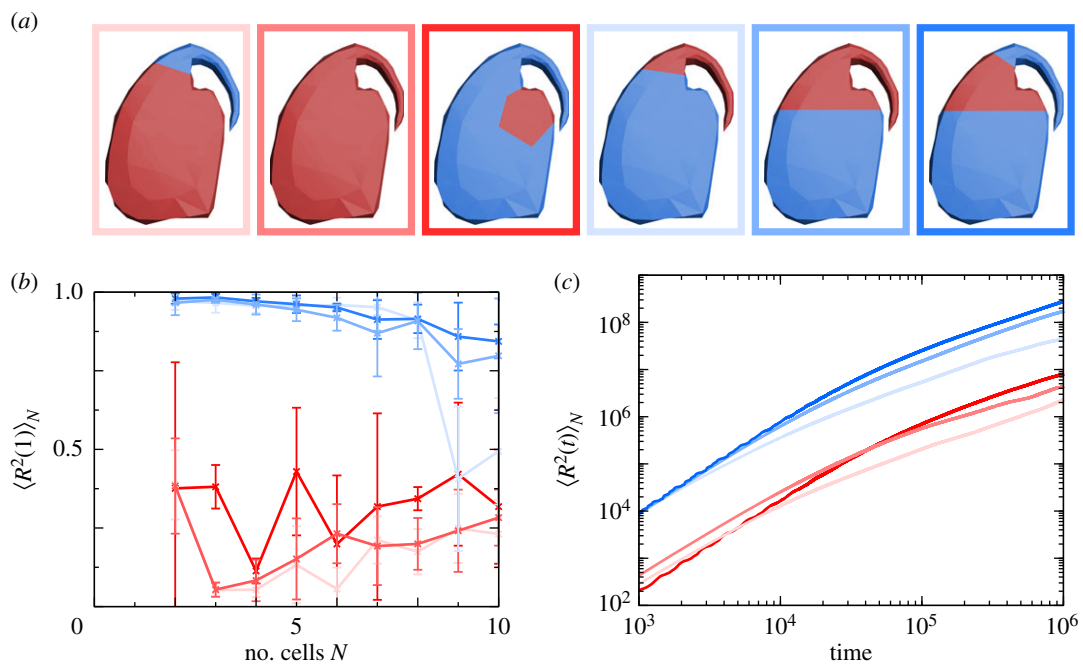
Figure 8. (a) The different adhesive regions that were simulated (in red). (b) Instantaneous speed of aggregates of four sperm depends strongly on the position of the adhesive region on the sperm head, colours correspond to the schematics above. (c) Mean square displacement of a group of four sperm with the accurate head shape ($t = 10^5$). Again, the position of the adhesive region greatly affects the efficiency of the aggregate.

effect and desegregation observed for the ellipsoidal sperm heads, resulting in generally more robust and efficient sperm aggregates.

4. Discussion and conclusion

Using numerical simulations, we have explored how the geometry of the sperm head affects the performance of aggregation. In our simulations, the sperm head is modelled as a persistent random walker characterized by a non-trivial three-dimensional shape. The head is further equipped with an adhesive region, where the cell binds to the head of other cells. Upon modelling the head via a simple parametric shape (i.e. an ellipsoid), we have established that the mobility of sperm aggregates is strongly affected by the head geometry. In particular, slender and oblate head shapes lead to

significantly faster aggregates compared to spherical head shapes, because they allow the cells to form tightly packed and highly polarized aggregates, thus reducing the spread in the velocities of the individual cells.

The structure of the adhesive region also has a profound impact on both the stability and the swimming performance of the aggregates. In particular, by simulating ellipsoidal heads endowed of adhesive strips of varying thickness and location, we find that some degree of internal flexibility is a vital feature for successful aggregation. When aggregates first form they typically do not have a polar structure and the cells tend to swim against each other. Cells having large adhesive areas are too tightly bound to their neighbours to reorient and eventually break apart. On the other hand, cells with smaller adhesive areas, such as a strip in the vicinity of the head equatorial plane, are sufficiently mobile to reorient in such a way that all the cells move toward the same direction. This enhances the stability of the aggregates as well as the persistence of their random motion.

Finally, most muroid rodents produce sperm with one or more hooks on the head of the cell [10]. Although the function of sperm hooks is unresolved, it has been hypothesized that the hook may interact with the epithelium of the female oviduct to aid sperm migration [31], may offer a hydrodynamic advantage to singly swimming cells [32], and/or may permit cells to attach to the hooks or flagellum of other sperm cells, thereby creating aggregates [11] (but see [33]). In this latter prediction, evidence suggests that sperm–sperm adhesion occurs along the inner surface of the hook in wood mice (*A. sylvaticus*) [2]. Our model suggests another alternative, that the hook acts as a shield in combination with an adhesive region localized at the acrosome or directly below at the equatorial segment. By shielding one side of the sperm head, the hook could favour the formation of aggregates in which all the cells have the same orientation, leading to more dense packing and a more effective alignment of the velocities of the interacting cells. This hypothesis is consistent with empirical observations of *Peromsycus* sperm [14] and numerical simulations (figure 8).

References

1. Parker GA. 1970 Sperm competition and its evolutionary consequences in the insects. *Biol. Rev.* **45**, 525–567. (doi:10.1111/j.1469-185X.1970. tb01176.x)

2. Moore H, Dvorakova K, Jenkins N, Breed W. 2002 Exceptional sperm cooperation in the wood mouse. *Nature* **418**, 174–177. (doi:10.1038/nature00832)

3. Pizzari T, Foster KR. Sperm sociality: cooperation, altruism, and spite. *PLoS Biol.* **6**, e130. (doi:10. 1371/journal.pbio.0060130)

4. Immler S. 2008 Sperm competition and sperm cooperation: the potential role of diploid and haploid expression. *Reproduction* **135**, 275–283. (doi:10.1530/REP-07-0482)

5. Fisher HS, Hoekstra HE. 2010 Competition drives cooperation among closely related sperm of deer mice. *Nature* **463**, 801–803. (doi:10.1038/ nature08736)

6. Higginson DM, Pitnick S. 2010 Evolution of intra-ejaculate sperm interactions: do sperm cooperate? *Biol. Rev.* **86**, 249–270. (doi:10.1111/j.1469-185X. 2010.00147.x)

7. Yang Y, Elgeti J, Gompper G. 2008 Cooperation of sperm in two dimensions: synchronization, attraction, and aggregation through hydrodynamic interactions. *Phys. Rev. E* **78**, 061903. (doi:10.1103/ PhysRevE.78.061903)

8. Tung C, Lin C, Harvey B, Fiore AG, Ardon F, Wu M, Suarez SS. 2017 Fluid viscoelasticity promotes collective swimming of sperm. *Sci. Rep.* **7**, 3152. (doi:10.1038/s41598-017-03341-4)

9. Schoeller SF, Keaveny EE. 2018 From flagellar undulations to collective motion: predicting the dynamics of sperm suspensions. *J. R. Soc. Interface* **15**, 20170834. (doi:10.1098/rsif.2017.0834)

10. Breed WG. 2005 Evolution of the spermatozoon in muroid rodents. *J. Morphol.* **265**, 271–290. (doi:10. 1002/jmor.10357)

11. Immler S, Moore HD, Breed WG, Birkhead TR. 2007 By hook or by crook? Morphometry, competition and cooperation in rodent sperm. *PLoS ONE* **2**, e170. (doi:10.1371/journal.pone.0000170)

12. Firman RC, Simmons LW. 2009 Sperm competition and the evolution of the sperm hook in house mice. *J. Evol. Biol.* **22**, 2505–2511. (doi:10.1111/j.1420-9101.2009.01867.x)

13. Han C, Kwon JT, Park I, Lee B, Jin S, Choi H, Cho C. 2010 Impaired sperm aggregation in *Adam2* and *Adam3* null mice. *Fertil. Steril.* **93**, 2754–2756. (doi:10.1016/j.fertnstert.2010.03.013)

14. Fisher HS, Giomi L, Hoekstra HE, Mahadevan L. 2014 The dynamics of sperm cooperation in a competitive environment. *Proc. R. Soc. B* **281**, 20140296. (doi:10.1098/rspb.2014.0296)

15. Vicsek T, Czirók A, Ben-Jacob E, Cohen I, Shochet O. 1995 Novel type of phase transition in a system of self-driven particles. *Phys. Rev. Lett.* **75**, 1226–1229. (doi:10.1103/PhysRevLett.75.1226)

16. Czirók A, Ben-Jacob E, Cohen I, Vicsek T. 1996 Formation of complex bacterial colonies via self-generated vortices. *Phys. Rev. E* **54**, 1791–1801. (doi:10.1103/PhysRevE.54.1791)

17. Couzin ID, Krause J, James R, Ruxton GD, Franks NR. 2002 Collective memory and spatial sorting in animal groups. *J. Theor. Biol.* **218**, 1–11. (doi:10. 1006/jtbi.2002.3065)

18. Buhl J, Sumpter DJT, Couzin ID, Hale JJ, Despland E, Miller EE, Simpson SJ. 2006 From disorder to order in marching locusts. *Science* **312**, 1402–1406. (doi:10.1126/science.1125142)

19. Chaté H, Ginelli F, Grégoire G, Peruani F, Raynaud F. 2008 Modeling collective motion: variations on the Vicsek model. *Eur. Phys. J. E* **64**, 451–456. (doi:10. 1140/epjb/e2008-00275-9)

20. Ballerini M *et al.* 2008 Interaction ruling animal collective behaviour depends on topological rather than metric distance: evidence from a field study. *Proc. Natl Acad. Sci. USA* **105**, 1232–1237. (doi:10. 1073/pnas.0711437105)

21. Peruani F, Starruß J, Jakovljevic V, Søgaard-Andersen L, Deutsch A, Bär M. 2012 Collective

motion and nonequilibrium cluster formation in colonies of gliding bacteria. *Phys. Rev. Lett.* **108**, 098102. (doi:10.1103/PhysRevLett.108.098102)

22. Vicsek T, Zafeiri A. 2012 Collective motion. *Phys. Rep.* **517**, 71–140. (doi:10.1016/j.physrep.2012.03.004)

23. Giomi L, Hawley-Weld N, Mahadevan L. 2013 Swarming, swirling and stasis in sequestered bristle-bots. *Proc. R. Soc. A* **469**, 20120637. (doi:10.1098/rspa.2012.0637)

24. Pearce DJG, Giomi L. 2016 Linear response to leadership, effective temperature and decision making in flocks. *Phys. Rev. E* **94**, 022612. (doi:10.1103/PhysRevE.94.022612)

25. Elgeti J, Winkler RG, Gompper G. 2015 Physics of microswimmers—single particle motion and collective behavior: a review. *Rep. Prog. Phys.* **78**, 056601. (doi:10.1088/0034-4885/78/5/056601)

26. *RAPID - Robust and accurate polygon interference detection*. URL: http://gamma.cs.unc.edu/OBB.

27. Moore HDM, Taggart DA. 1995 Sperm pairing in the opossum increases the efficiency of sperm movement in a viscous environment. *Biol. Reprod.* **52**, 947–953. (doi:10.1095/biolreprod52.4.947)

28. Moore HDM. 1996 Gamete biology of the New World marsupial, the grey short-tailed opossum, *Monodelphis domestica*. *Reprod. Fert. Develop.* **8**, 605–615. (doi:10.1071/RD9960605)

29. Hayashi F. 1998 Sperm co-operation in the fishfly, *Parachauliodes japonicus*. *Funct. Ecol.* **12**, 347–350. (doi:10.1046/j.1365-2435.1998.00205.x)

30. Guidobaldi A, Jeyaram Y, Berdakin I, Moshchalkov VV, Condat CA, Marconi VI, Giojalas L, Silhanek AV. 2015 Geometrical guidance and trapping transition

of human sperm cells. *Phys. Rev. E* **89**, 032720. (doi:10.1103/PhysRevE.89.032720)

31. Suarez SS. 1987 Sperm transport and motility in the mouse oviduct: observations *in situ*. *Biol Reprod.* **36**, 203–210. (doi:10.1095/biolreprod36.1.203)

32. Gómez Montoto L, Sánchez MV, Tourmente M, Martín-Coello J, Luque-Larena JJ, Gomendio M, Roldan ERS. 2011 Sperm competition differentially affects swimming velocity and size of spermatozoa from closely related muroid rodents: head first. *Reproduction* **142**, 819–830. (doi:10.1530/REP-11-0232)

33. Tourmente M, Zarka-Trigo D, Roldan ERS. 2016 Is the hook of muroid rodent's sperm related to sperm train formation? *J. Evol. Biol.* **29**, 1168–1177. (doi:10.1111/jeb.12857)